Critical heat flux in a long, curved channel subjected to concave heating

J. Christopher Sturgis, Issam Mudawar*

Boiling and Two-Phase Flow Laboratory, School of Mechanical Engineering, Purdue University, West Lafayette, IN 47907, USA

Abstract

A theoretical model to predict critical heat flux in long, rectangular, curved channels is presented. Development is analogous to a model for long, straight channels previously proposed by the present authors. The model is based on the observation from a flow visualization study that vapor assumes a wavy, periodic distribution along the heated concave wall just prior to CHF such that liquid–surface contact is restricted to the troughs of the wave, called wetting fronts. When the idealized oscillatory liquid–vapor interface is lifted off the surface liquid can no longer rewet the surface to remove heat and CHF ensues. This lift-off of the interface occurs when vapor momentum emanating from a wetting front due to vigorous boiling overcomes the pressure force which serves to hold the interface in contact with the surface. A separated flow model, interfacial instability analysis, heater energy balance, lift-off criterion and flow visualization study combine to form a mechanistically-based CHF model for long, curved surfaces. The model predicts curved channel CHF data to within a mean absolute error of only 4.0% at near-saturated conditions for velocities up to 10 m s^{-1}, corresponding to centripetal accelerations reaching 315 times Earth's gravitational acceleration. The model accurately reflects the enhancement in CHF that curvature provides by offering predictions that are greater than the corresponding straight channel model predictions. © 1999 Elsevier Science Ltd. All rights reserved.

1. Introduction

Enhancement of critical heat flux (CHF) is highly desirable in that it increases the thermal limit at which many thermal devices catastrophically fail. Streamwise flow curvature with concave heating has been shown to enhance the critical heat flux compared to straight channel flow [1–4], in some cases up to 70%. The difficult issue in applying this benefit is knowing the enhanced CHF limit. Predictions of such a limit would permit thermal devices to take advantage of the

broader heat flux range while still maintaining appropriate safety margins. For example, this would help electronics cooling schemes keep pace with the constantly increasing heat dissipation rates associated with advancing microelectronic packaging technologies. Correlations of existing CHF data could be used to estimate the enhanced limit but may be restricted by the test conditions under which the data were obtained. A model is more desirable since it would not only offer mechanistically-based predictions, allowing for consideration of different test conditions, but would also provide insight into which parameters influence CHF the most.

With this perspective, a model was developed in the present study to predict CHF data obtained in a curved flow channel over broad ranges of velocity and

* Corresponding author. Tel.: +1-765-494-5705; fax: +1-765-494-0539.

E-mail address: mudawar@ecn.purdue.edu (I. Mudawar)

Nomenclature

A_f	cross-sectional area of liquid phase
A_g	cross-sectional area of vapor phase
A_l	area of wetting front
b	ratio of liquid length to vapor wavelength, l/λ
c	wave speed
c_i	imaginary component of wave speed
$C_{f,i}$	interfacial friction coefficient
$c_{p,f}$	liquid specific heat at constant pressure
c_r	real component of wave speed
d_{up}	distance from heater inlet to trailing edge of vapor patch
D_h	channel hydraulic diameter
$D_{h,k}$	hydraulic diameter of phase identified by k
f	single-phase friction factor
F_f	pressure force acting on face of liquid control volume
F_g	pressure force acting on face of vapor control volume
g^*	centripetal acceleration non-dimensionalized by g_e
g_e	Earth's gravitational acceleration
g_n	body force per unit mass normal to surface
h_{fg}	latent heat of vaporization
H	channel height
H_f	liquid layer thickness
H_g	vapor layer thickness
k	wave number, $2\pi/\lambda$
k_{cr}	critical wave number, $2\pi/\lambda_{cr}$
l_j	length of wetting front in heater segment j
l_{meas}	measured liquid length between vapor patches
L	length of heater
L_j	length of heater segment j
n_j	number of wetting fronts in heater segment j
P	pressure
$\overline{P_f - P_g}$	average pressure difference acting over the wetting front
q''	heat flux
q''_j	average wetting front heat flux for heater segment j
q''_l	heat flux concentrated at a wetting front
$q''_l(z^*)$	wetting front heat flux based on conditions at z^*
q''_m	maximum nucleate boiling heat flux, CHF
r	radial coordinate in curved heater
Re_D	Reynolds number based on diameter (geometric or hydraulic)
R_0	radius of unperturbed liquid–vapor interface
R_1	radius of inner wall of curved channel
R_2	radius of outer wall of curved channel
t	time coordinate
T_{sat}	fluid saturation temperature at outlet of heated section
U	average inlet liquid velocity
$\bar{U}_f$	mean velocity of liquid phase
$\bar{U}_{f,i}$	mean velocity component of liquid phase at interface
$\bar{U}_g$	mean velocity of vapor phase
$\bar{U}_{g,i}$	mean velocity component of vapor phase at interface
$U_{g,n}$	vapor velocity in wetting front normal to surface
W	channel width
y	coordinate perpendicular to unperturbed interface
z	streamwise coordinate, $z = 0$ at heater inlet

z^*	extent of upstream continuous wetting front
z_0	distance from inlet to where $\bar{U}_f = \bar{U}_g$

Greek symbols

δ	mean vapor layer thickness ($\delta = H_g$), vapor layer amplitude for CHF modeling
δ_{meas}	measured vapor patch height
ΔT_{sub}	fluid subcooling
$\Delta T_{\mathrm{sub,o}}$	fluid subcooling at outlet of heated section at CHF
η	idealized sinusoidal perturbation of interface
η_0	maximum amplitude of sinusoidal perturbation, $\eta_0 = \delta$
θ	turn angle of flow, measured from beginning of curvature
λ	vapor wavelength for CHF modeling
λ_{cr}	critical wavelength
λ_{meas}	measured vapor patch length
μ	dynamic viscosity
ρ	density
ρ'''_k	modified density term for phase identified by k
σ	surface tension
τ_i	interfacial shear stress
$\tau_{\mathrm{w},k}$	shear stress between wall and phase identified by k

Subscripts

A	acceleration
C	centrifugal (curvature)
F	frictional
f	saturated liquid
g	saturated vapor
i	interface
j	indicates heater segment, $j = 1, 2, 3, 4$
k	indicates phase, $k = f$ for liquid, $k = g$ for vapor
str	straight channel

subcooling. The configuration of interest is a rectangular channel with heat applied only to the concave wall over a long length with a thick-walled heater.

Several researchers have demonstrated experimentally the enhancement provided by streamwise curvature, though discrepancies exist regarding the effects of centripetal acceleration and subcooling. Hughes and Olson [1], Sturgis and Mudawar [4], Leland and Chow [5] and Wu and Simon [6] have demonstrated that the ratio of curved-to-straight channel CHF decreases with increases in subcooling, though test conditions among the researchers varied: Hughes and Olsen [1] used R-113 fluid with long, thin ribbon heaters; Sturgis and Mudawar [4] tested with FC-72 fluid and long, thick heaters; Leland and Chow [5] used FC-72 but a discrete, thick heater positioned at the 135° position on the concave wall; Wu and Simon [6] tested with FC-72 using a discrete, thick heater in a wide channel. Leland and Chow [5] actually showed a detrimental curvature effect for high subcooling ($\Delta T_{\mathrm{sub}} = 35°C$) in a channel with a concave wall radius of curvature of $R_2 = 28.6$ mm.

Gu et al. [3] found the enhancement ratio to be proportional to centripetal acceleration to the 0.785 power while Gambill and Green [7] deduced the exponent to be between 0.43 and 0.48. The former case was for a discrete heater on the channel's concave wall with centripetal acceleration ranging from 2–32 times Earth's gravitational acceleration, g_e; the latter involved tangential inflow into a tube (swirl flow) encompassing conditions up to $8390g_e$. In contrast, Sturgis and Mudawar [4] presented enhancement ratios (for long heaters) that tended toward constant values, which depended on outlet subcooling, for centripetal accelerations reaching $315g_e$.

Hughes and Olson [1] proposed a model to predict subcooled critical heat fluxes from straight, convex and concave surfaces based on the concept that vapor bubbles completely cover the heated surface at CHF. With each active nucleation site they associated an area proportional to the diameter of the departing bubble. They postulated that when a critical packing density is reached—that is, when the sum of these areas equals the total surface area of the heater—no

Four Heater Segments
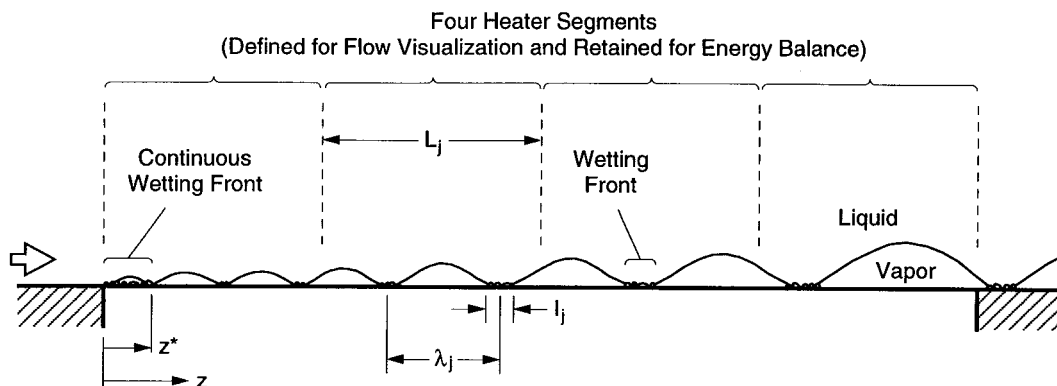**(Defined for Flow Visualization and Retained for Energy Balance)**

Fig. 1. Idealized wavy liquid–vapor interface showing vapor and liquid definitions and heater segments.

additional nucleation sites can be activated and CHF ensues.

Galloway and Mudawar [2,8] developed the interfacial lift-off model to predict CHF from short curved and straight surfaces. They noted from their flow visualization study that just prior to CHF the vapor assumed a wavy, periodic distribution along the surface with liquid contacting the heated wall at the troughs of the wave. They proposed that CHF occurred when this wavy interface was lifted off which resulted from the vigorous boiling at a wetting front overcoming the pressure force holding the interface in contact with the surface. This restricted liquid rewetting of the surface prompting CHF. They predicted their straight and curved experimental data to within mean absolute errors of 7 and 14%, respectively. However, they noted that their assumptions limited the model to conditions of low centripetal accelerations ($g^* < 10$) and short heaters ($L \approx 12.7$ mm).

The present work extends the curved model of Galloway and Mudawar to higher accelerations (315 g_e) and long heaters ($L \approx 100$ mm) while offering other subtle refinements. It draws upon the interfacial lift-off criterion first proposed by Galloway and Mudawar [8] and follows a development similar to the CHF model proposed by the present authors for flow in long, straight rectangular channels [9].

2. CHF model for long, straight channels

The models presented here for flow in long, straight and curved channels are based on the observation that at conditions just prior to CHF the vapor assumes a periodic, wave-like distribution along the heater surface, which is idealized by the wavy liquid–vapor interface depicted in Fig. 1 for straight flow. The models are constructed from four components—separated flow model, instability analysis, energy balance and lift-off

criterion—which combine to yield an iterative procedure for predicting CHF. Additionally, flow visualization provides several key contributions. Model construction and assumptions are similar for straight and curved flow with the main differences arising in the separated flow model, instability analysis and flow visualization results due to the effect of curvature. The straight channel model is outlined here but described in greater detail in Ref. [9].

The two-phase flow is analyzed by assuming the phases remain separate with each characterized by a mean velocity. Due to boiling at the surface, mass is continually added to the vapor layer such that the mean vapor thickness increases along the flow direction. Due to the density disparity between the phases, the mean vapor velocity, $\bar{U}_g$, tends to increase rapidly, surpassing the mean liquid velocity, $\bar{U}_f$. This velocity difference leads to the interfacial instability that has been visualized at CHF conditions. The separated flow model contributes values for the phase velocities and average vapor thickness to the instability analysis.

The wavy interface depicted in Fig. 1 becomes unstable under particular conditions related to phase velocity difference, vapor thickness, surface tension, densities and normal body force. The goal of the instability analysis is to predict the circumstances at which the wavy interface is neutrally stable, characterized by a critical wavelength, since an interface at this point would be most susceptible to the vapor momentum flux associated with vigorous boiling at a wetting front. The primary contribution of the instability analysis then is the calculation of the critical wavelength, λ_{cr}. Additionally, it determines the length of the continuous upstream wetting front, z^*, from the relation

$$z^* = z_0 + \lambda_{cr}(z^*). \tag{1}$$

This upstream wetting front is a region of continual

liquid–surface contact (vapor has yet to coalesce enough to impeded liquid rewetting) and extends one critical wavelength past z_0, which is the location along the heater where the phase velocities are equal, $\bar{U}_g = \bar{U}_f$, based on separated flow model calculations. Beyond z_0, which in the present case is typically less than 5% of heater length, the velocity difference increases promoting instability.

The energy balance draws on the idealization of the wavy interface which limits liquid contact with the surface to discrete locations referred to as wetting fronts. It is in these locations that all heat transfer to the liquid occurs while the surface beneath a vapor wave is assumed adiabatic. Therefore, knowing the length and number of wetting fronts is crucial to obtaining an accurate description of heat transfer. The heated length was partitioned into four segments for the flow visualization study described in [9] and this segmentation was retained for the construction of the energy balance. In this manner, the energy balance is able to account for the continuous stretching of the wavelength by using different average vapor lengths for segment, essentially discretizing the heated length. Likewise, the length and number of wetting fronts are accounted for in each segment. In this way, the CHF model is able to reflect the physical observations by including the averages of measured interfacial characteristics.

The energy balance states that the sum of energy dissipated at all wetting fronts (including the continuous upstream wetting front) is equal to the energy dissipated by an average flux acting over the entire heated surface. This average flux is regard as the critical heat flux, q_m'', for the heater. Therefore, the energy balance yields the expression

$$q_m'' = \frac{1}{L - z^*}[q_1'' l_1 n_1 + q_2'' l_2 n_2 + q_3'' l_3 n_3 + q_4'' l_4 n_4] \tag{2}$$

where l_j is the average wetting front length and n_j is the number of wetting fronts, each defined for the jth segment, where j takes the values 1, 2, 3 or 4 depending on the segment being referenced. The average flux at a wetting front in segment j is denoted by q_j''. The z^* term accounts for the continuous upstream wetting front where a flux equal to the critical heat flux is assumed. This is based on the notion that in the absence of vapor patches on the surface, the flux at any location along the heater would be equal to the critical heat flux. But vapor impedes the heat transfer from the surface resulting in higher concentrations at wetting fronts, except in the continuous wetting region at the inlet where the flux is approximated as the critical heat flux since it is assumed the heat flow path to the fluid is not significantly affected. In the curved channel, streamwise dimensions are measured along

the heated wall so that this energy balance uses the same definitions for vapor and liquid lengths. Hence, Eq. (2) applies to the curved model as well since consistent definitions for L, z^*, l_j and n_j are employed.

The number of wetting fronts in a given heater segment is defined by

$$n_j = \begin{cases} \dfrac{L_1 - z^*}{\lambda_1} & \text{for } j = 1 \\[2mm] \dfrac{L_j}{\lambda_j} & \text{for } j = 2, \ 3, \ 4 \end{cases} \tag{3}$$

where L_j is the length of the segment and λ_j the average wavelength characterizing the jth segment, as indicated in Fig. 1. n_j is allowed to take on fractional values, as opposed to strictly integer values, in order to extend an instantaneous energy balance to account for average conditions. The average number of wetting fronts in a given heater segment over time is more accurately represented by the relations given in Eq. (3) without truncating the remainder.

Values for wetting front length, l_j, are based on flow visualization measurements which indicate wetting front length remains proportional to the local wavelength. In this way, l_j is referenced to the local wavelength by the ratio b, defined by

$$b = \frac{\text{wetting front length}}{\text{vapor wavelength}} = \frac{l_j}{\lambda_j}. \tag{4}$$

Therefore, wetting front length can be calculated from knowledge of vapor wavelength and the ratio b. Additionally, flow visualization measurements described in [9] indicated that for both straight and curved flow, this ratio of wetting front length to vapor wavelength remains constant along the flow direction and for velocities (1–4 m s^{-1} experimental range) with the same outlet subcooling. This result simplifies the energy balance.

Since wetting front length increases proportionately with vapor wavelength, the product $(l_j n_j)$ allows the energy balance to proceed without specific knowledge of the vapor wavelength. Using Eqs. (3) and (4) to express this product yields for the first segment,

$$l_1 n_1 = (b\lambda_1)\frac{L_1 - z^*}{\lambda_1} = b(L_1 - z^*) \tag{5a}$$

and for the downstream segments ($j = 2, 3, 4$),

$$l_j n_j = (b\lambda_j)\frac{L_j}{\lambda_j} = bL_j. \tag{5b}$$

Therefore, the need to have a predictive expression for vapor wavelength for all conditions is alleviated. This has beneficial consequences for the model development—by assuming that ratio of wetting front length
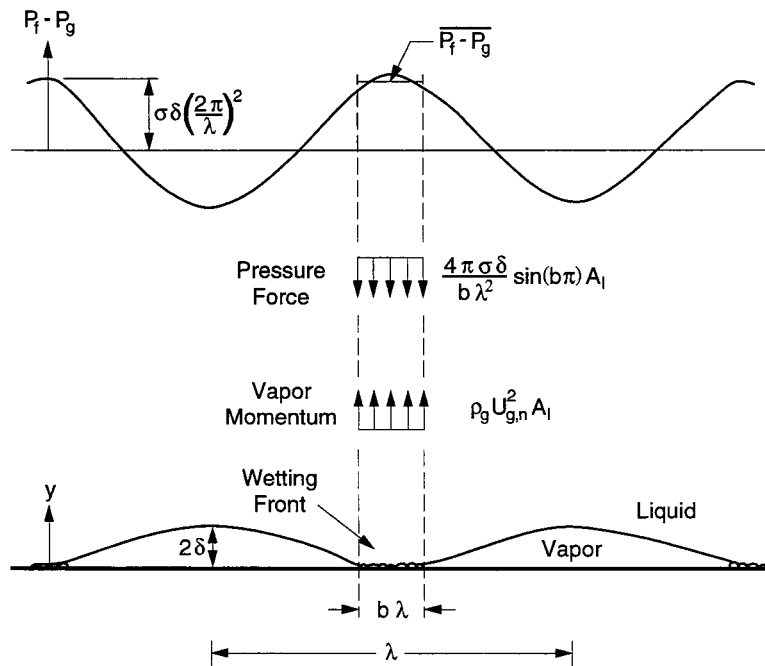
Fig. 2. Average pressure difference and vapor momentum at wetting front used to determine lift-off heat flux.

to vapor wavelength is constant along a heater and with increasing velocity, the modeling effect may be extended to velocities beyond which flow visualization was performed.

The energy balance for the straight channel [Eq. (2)] applies directly to curved flow in which case the values for z^*, q_j'', b and n_j reflect the curvature effects.

The lift-off criterion provides the relationship for determining the fluxes concentrated at the wetting fronts, q_j''. CHF is postulated to occur when the momentum flux of vapor emanating from the surfaces overcomes the pressure force tending to maintain interfacial contact with surface [10] as depicted in Fig. 2. This results in detachment of the interface at that wetting front and elimination of heat transfer to the fluid. The remaining wetting fronts must accommodate this loss which increases the other local fluxes resulting in more vigorous boiling and interfacial lift-off at these locations as well. Therefore, critical heat flux is identified by the imbalance between vapor momentum and pressure force. Galloway and Mudawar postulated that the lift-off of the most upstream wetting front is the trigger mechanism for CHF and the flow visualization results of Gersey and Mudawar [11] support this conclusion. Therefore, the wetting front fluxes indicated in the energy balance are approximated as the flux sufficient to detach a wetting front located at z^*.

An expression for the lift-off flux at any wetting front, q_l'', may be determined by equating the pressure

force acting to maintain interfacial contact with the vapor momentum tending to push the interface away as illustrated in Fig. 2. The force is approximated by averaging the pressure difference acting at a wetting front over the length of the wetting front, $b\lambda$. This difference in vapor and liquid pressures across a curved interface may be expressed, for mild curvature, as the product of surface tension and interfacial curvature. For the assumption of a sinusoidal interface, the average pressure difference is

$$\overline{P_f - P_g} = \frac{4\pi\sigma\delta}{b\lambda^2}\sin(b\pi). \qquad (6)$$

Vapor momentum is a product of vapor density and the normal velocity, $U_{g,n}$, which is evaluated from an energy balance at the wetting front where the entire local flux, q_l'', is responsible for converting a mass of slightly subcooled liquid to saturated vapor. Equating these force and momentum terms, identified in Fig. 2, results in an expression for lift-off flux,

$$q_l'' = \rho_g(c_{p,f}\Delta T_{sub} + h_{fg})\left[\frac{\overline{P_f - P_g}}{\rho_g}\right]^{1/2} \qquad (7)$$

where $\overline{P_f - P_g}$ is given by Eq. (6). The lift-off flux evaluated at z^*, $q_l''(z^*)$, used in the energy balance, is evaluated from Eqs. (6) and (7) with $\delta = \delta(z^*)$ and $\lambda = \lambda_{cr}$.
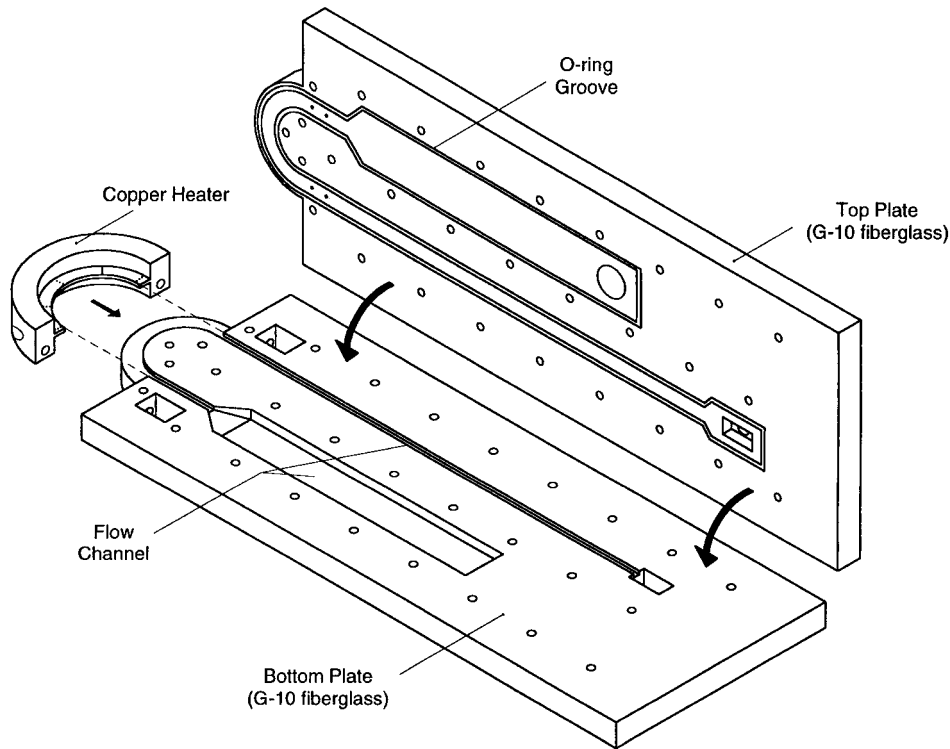
Fig. 3. Assembly view of curved channel showing heater and G-10 fiberglass plates.

The energy balance, Eq. (2), can now yield an expression for CHF. Substituting the products $(l_j n_j)$ given by Eq. (5) and noting that $q''_j = q''_l(z^*)$, the critical heat flux, q''_m, reduces to

$$q''_m = b q''_l(z^*). \tag{8}$$

This expression holds for long straight and curved heaters with the differences in CHF predictions attributed to separated flow model, stability analysis and flow visualization results. It states that the fluxes concentrated at the wetting fronts are greater than the critical heat flux by the factor $1/b$ since the latter is taken as an average value acting over the entire heated surface. This expression yields a CHF prediction as a product of a theoretically-based term, $q''_l(z^*)$, and a physically measured term, b.

3. Experimental methods

The channel used in this curved flow CHF investigation was comprised of three pieces—two plates of opaque, high temperature, low thermal conductivity ($k = 0.26$ W m^{-1} K^{-1}) G-10 fiberglass and a copper heater, all shown in Fig. 3. In the bottom G-10 plate was machined a 5.0×2.5-mm rectangular cross-section

groove which made a 180° turn forming a U-shaped channel. The concave wall was removed and replaced with a 99.99% oxygen-free copper heater which was bolted to the plate such that its surface was flush with the straight walls of the channel. The top G-10 plate closed out the channel when placed on top, forming a tight seal. The heated surface, measuring 2.5 mm wide and 101.6 mm along the flow direction with a 32.3 mm radius, was preceded by a hydrodynamic entry length of 106 hydraulic diameters. The geometry of the flow channel and heated section is indicated in Fig. 4.

Five sets of three thermocouples were placed in the copper heater as shown in Fig. 4 in order to determine local wall heat flux, q'', and wall temperature along the flow. The beads of Type-K thermocouples (0.33 mm diameter) were epoxied into the three holes (0.25 mm diameter, 1.52 mm depth) which were precisely drilled with respect to each other and the heated surface. From the thermocouple readings, a logarithmic temperature profile was constructed assuming one-dimensional conduction through the thin, instrumented portion. Given the profile, wall flux and wall temperature were easily calculated with the assumption of constant copper conductivity (391 W m^{-1} K^{-1}). Power was supplied to the heater by five cylindrical cartridge heaters embedded in the thick portion of the copper. Distributing them as indicated and using a high con-
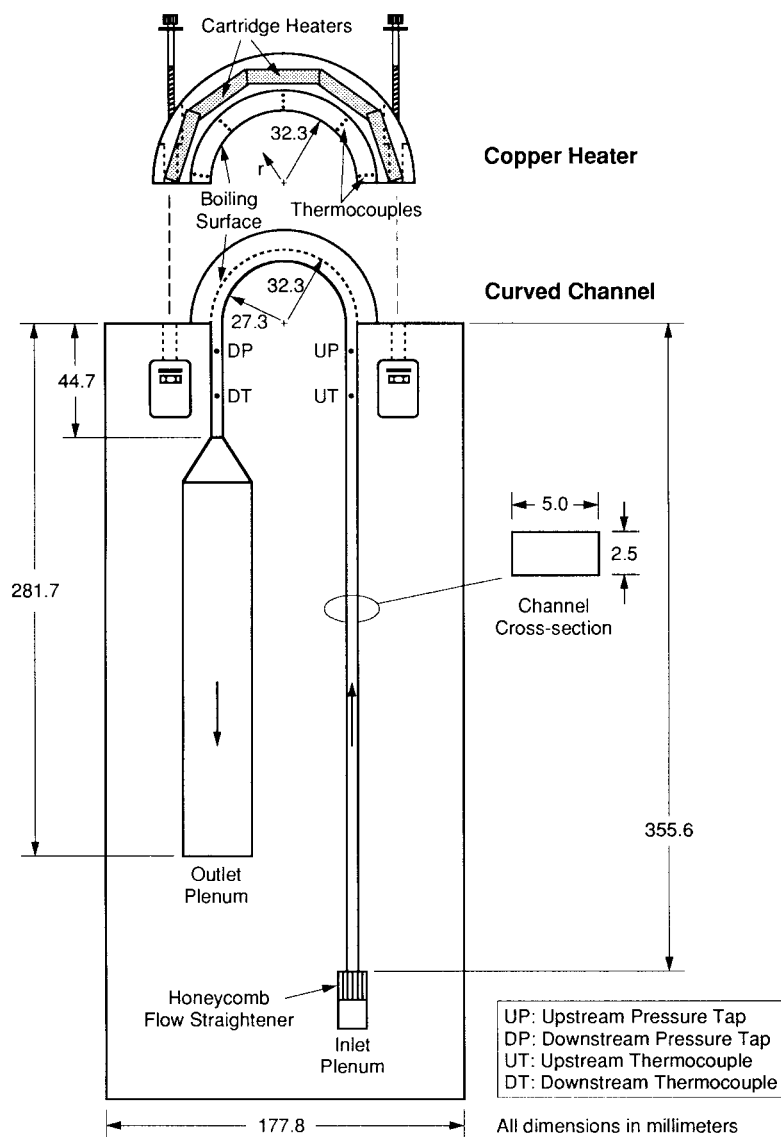
Fig. 4. Curved heater and bottom plate of curved channel.

ductivity material for the heater ensured power was evenly applied along the heated length.

The channel/heater assembly was tested in a closed two-phase flow loop using degassed FC-72, a dielectric Fluorinert manufactured by 3M Company. Its low boiling point (57°C at 1 atm) and relatively low heat of vaporization required only a modest heat input to achieve boiling. Properties of FC-72 for the near-saturated test condition (1.38 bar) are: $\rho_f = 1580$ kg m^{-3}; $\rho_g = 15.4$ kg m^{-3}; $\mu_f = 4.1 \times 10^{-4}$ kg m^{-1} s^{-1}; $\mu_g = 1.2 \times 10^{-5}$ kg m^{-1} s^{-1}; $h_{fg} = 91{,}100$ J kg^{-1}; $c_{p,f} = 1110$ J kg^{-1} K^{-1}; $\sigma = 7.4 \times 10^{-3}$ N m^{-1}; and $T_{sat} = 66.3°C$.

Critical heat flux, q''_m, was defined as the largest flux

attained under steady conditions. Since at CHF a vapor blanket essentially insulated the surface, heat supplied by the cartridge heaters was no longer transferred to the liquid but rather built up in the copper to cause a temperature rise and gradient decrease. Therefore, CHF was detected by closely monitoring the data for an unsteady increase in calculated wall temperature accompanied by an abrupt decrease in calculated wall flux.

These heat transfer tests were conducted with outlet subcooling $(\Delta T_{sub,o} = 3°C)$ and mean velocity $(U = 0.25–10$ m s$^{-1})$ as controlled parameters. $\Delta T_{sub,o}$ is defined as the difference between outlet saturation
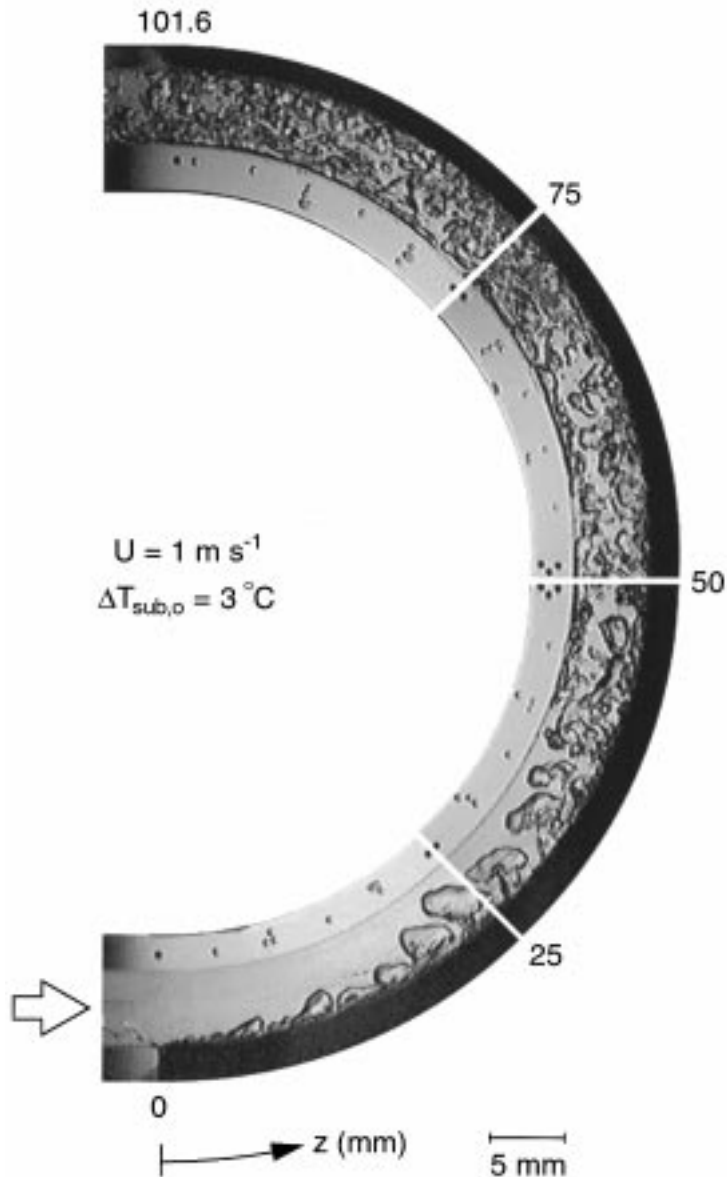
Fig. 5. Video images of flow boiling at CHF in curved channel at $U = 1$ m s^{-1} for near-saturated ($\Delta T_{\text{sub,o}} = 3°$C) conditions.

temperature, T_{sat}, and outlet bulk temperature at the time of critical heat flux. Inlet subcooling, an independent parameter, varied between 7 and 12°C for velocities $U \geq 0.5$ m s^{-1}. The Reynolds number defined in terms of hydraulic diameter and inlet properties, $Re_{\text{D}} = \rho_f U D_{\text{h}}/\mu_f$, ranged from 2000 to 130,000. Over the same range, mass flux varied from 400 to 16,800 kg m^{-2} s^{-1} and centripetal acceleration, g^*, 0–315, where

$$g^* = \frac{U^2}{R_2 g_{\text{e}}}. \tag{9}$$

Numerical modeling revealed that heat losses from the thin, instrumented portion of the heater represented less than 5% of the heat flowing into this portion; for this reason, losses were neglected in calculations. For 18 of 19 conditions with multiple tests, all CHF values differed from their respective averaged by less than 2.6%. This was within the uncertainty in heat flux, which was approximately 8.5% at low fluxes ($q'' \approx 30$ W cm^{-2}) decreasing to less than 5% at high fluxes ($q'' \approx 150$ W cm^{-2}). Wall temperature calculations were accurate to within 0.3°C and flowrate uncertainty was
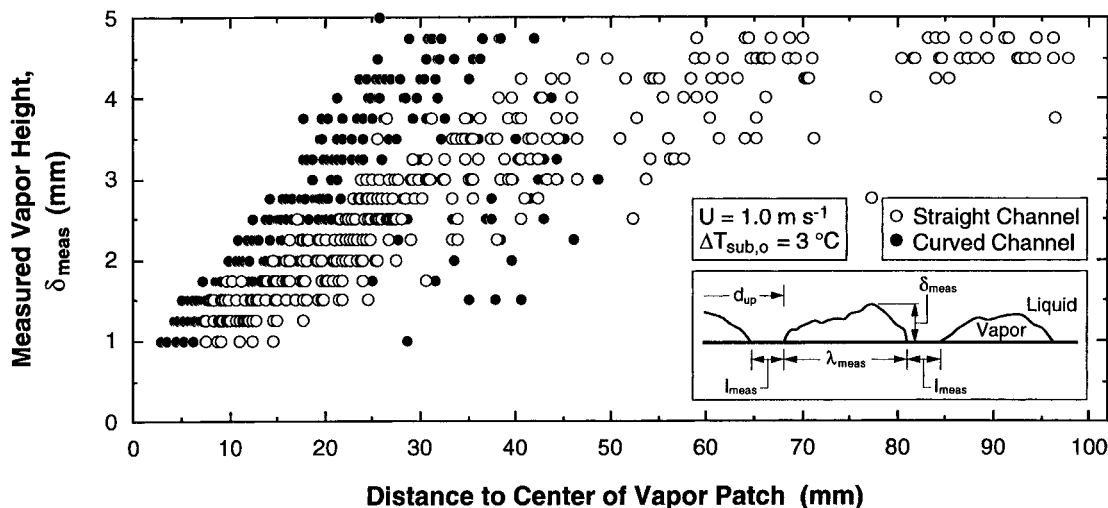
Fig. 6. Measured heights of vapor patches at CHF in straight and curved channels for $U = 1$ m s^{-1} and near-saturated ($\Delta T_{sub,o} = 3°C$) conditions.

less than 2.3%. More discussion of experimental methods may be found in Ref. [4].

4. Flow visualization in curved channel

Flow visualization tests conducted in the curved channel permitted the observation of vapor development and the measurement of vapor and liquid characteristics. Boiling dynamics were captured along the entire heated length for various velocity and subcooling conditions using a Canon L1 8-mm video camera and a transparent channel identical in design to that used to obtain the CHF data. A more complete description of flow visualization techniques is presented in Ref. [12].

Vapor patches in the curved channel were observed to be distributed in a periodic, wavy pattern on the upstream segment as shown in Fig. 5. In this image, flow is counterclockwise with the heater along the concave wall. A distinguishing difference between straight and curved flow is the buoyancy force which arises from the radial pressure gradient in curved flow. This force pulls the vapor inward, elongating a vapor patch such that its height, measured normal to the surface, is greater in the first segment of the curved channel than at a corresponding location in the straight. This is evidenced by the numerous measurements of vapor height, δ_{meas}, plotted in Fig. 6 against distance from the inlet to center of a measured vapor patch for near-saturated conditions. The larger measured heights in the curved channel are idealized by a larger interfacial amplitude, δ, resulting in greater average pressure

difference [Eq. (6)], lift-off flux [Eq. (7)] and, ultimately, critical heat flux [Eq. (8)].

Farther downstream, the buoyancy forces continue to pull on the vapor patches eventually breaking off portions as shown in Fig. 5. These fragments are then distributed through the cross-section while the vapor patches remaining on the surface are reduced in size. This break-up of vapor made observing and measuring vapor dimensions downstream difficult for some conditions resulting in incomplete data for vapor and liquid measurements along the curved heater.

However, the construction of the energy balance circumvents this difficulty in that it utilizes the lift-off heat flux based on conditions upstream at z^*, which is typically less than 5 mm, at which point the wavy shape is observed. Furthermore, based on measurements that were obtained, the liquid-to-vapor length ratio was found to be approximately constant along the flow direction and for velocities with the same subcooling. The assumption is made that this ratio is preserved along the heater and at higher velocities than for which vapor measurements were obtained. This result and assumption are instrumental in enabling the present model to cover a broader range of velocity on a longer heater as compared to the curved CHF model proposed by Galloway and Mudawar [2].

Extensive vapor measurements indicate that the value of the liquid-to-vapor length ratio, b, increases for subcooled conditions and for curved flow. This indicates that subcooling and curvature are better able to break up the vapor layer and allow more liquid to contact the surface. The CHF model is able to reflect these trends by incorporating this ratio. Table 1 gives

Table 1
Liquid-to-vapor length ratios, b, based on flow visualization and utilized in model predictions

	Near-saturated ($\Delta T_{\text{sub,o}} = 3°C$)	Subcooled ($\Delta T_{\text{sub,o}} = 29°C$)
Straight channel	0.20	0.30
Curved channel	0.27	0.35

these liquid-to-vapor length ratios which are used in the model predictions.

5. CHF model for long, curved channels

5.1. Separated flow model

The separated flow analysis for the curved, rectangular channel employs the same assumptions as in the straight channel model with the main difference being a radial pressure gradient affecting the momentum balances. Therefore, conservation of mass and energy yield the same results. Boiling at the surface adds mass to the vapor phase and the resulting expressions for mean vapor and liquid velocities are given, respectively, by

$$\bar{U}_g = \frac{q'' R_2 \theta}{\rho_g \delta [c_{p,f} \Delta T_{\text{sub}} + h_{fg}]} \qquad (10)$$

and

$$\bar{U}_f = \frac{UH}{H - \delta} - \frac{q'' R_2 \theta}{\rho_f (H - \delta)[c_{p,f} \Delta T_{\text{sub}} + h_{fg}]} \qquad (11)$$

where $z = R_2 \theta$, $H = R_2 - R_1$ and $\theta = 0$ at the leading edge of the heater.

The momentum and force terms are shown for the vapor control volume in Fig. 7(a) and for the full channel control volume in Fig. 7(b). The terms located at the control surfaces are evaluated by means of Taylor series expansions about the angular center of the control volumes. The interfacial shear (τ_i) is assumed to act solely in the streamwise direction and wall shear ($\tau_{w,g}$ and $\tau_{w,f}$) is accounted for on the concave, convex and side walls. The pressure forces acting at the inner and outer walls are in the radial direction and do not contribute to the streamwise conservation equations. Also, vapor generated at the wall is assumed to have no initial streamwise velocity and, as such, does not contribute to the streamwise momentum balance.

The force terms, F_g and F_f, acting on the control volumes account for the effects of the curvature-induced radial pressure gradient, which increases radially outward. Since the vapor layer is thin and has low density, it is a reasonable approximation to con-

sider vapor pressure constant with respect to r,

$$F_g \approx P_g W \delta. \qquad (12)$$

However, this is not the case for the liquid. This is analogous to the contrast in hydrostatic pressure increases through air and water. The force F_f acting on the liquid is evaluated from the integration of pressure across the liquid layer such that

$$F_f = \int_{R_1}^{R_2 - \delta} P_f(r) W \, \mathrm{d}r. \qquad (13)$$

F_f is evaluated by first determining the radial pressure distribution using Euler's equation in the radial direction. Assuming uniform liquid velocity across the layer and noting that at the interface $r = R_2 - \delta$ and $P_f = P_i$, integration of the pressure distribution yields

$$F_f = P_i(H - \delta)W - \rho_f \bar{U}_f^2 W \left[(H - \delta) - R_1 \ln\left(\frac{R_2 - \delta}{R_1}\right) \right]. \qquad (14)$$

Conservation of momentum applied to the vapor control volume (Fig. 7(a)) and the entire two-phase mixture (Fig. 7(b)) yields pressure gradient terms which provide the constraint leading to the solution for phase velocities, $\bar{U}_g$ and $\bar{U}_f$, and vapor thickness, δ, at each streamwise location z. Applying momentum conservation, substituting relations given in Eqs. (12) and (14), converting angular derivative to derivatives with respect to heated length ($\partial/\partial\theta = R_2 \, \partial/\partial z$), assuming the geometry is such that $\delta/R_2 \ll 1$ and $(H - \delta)/(2R_1) \ll 1$, and noting that $A_g = W\delta$, $A_f = (H - \delta)W$ and $P_g = P_i$ (pressure is constant across vapor layer), the vapor and interfacial pressure gradients may be expressed, respectively, by

$$-\frac{\mathrm{d}P_g}{\mathrm{d}z} = \frac{\rho_g}{\delta} \frac{\mathrm{d}}{\mathrm{d}z}[\bar{U}_g^2 \delta] + \tau_{w,g}\left[\frac{1}{\delta} + \frac{2}{W}\right] + \frac{1}{\delta}\tau_i \qquad (15)$$

and

$$-\frac{\mathrm{d}P_i}{\mathrm{d}z} = \left(-\frac{\mathrm{d}P_i}{\mathrm{d}z}\right)_A + \left(-\frac{\mathrm{d}P_i}{\mathrm{d}z}\right)_F + \left(-\frac{\mathrm{d}P_i}{\mathrm{d}z}\right)_C \qquad (16)$$
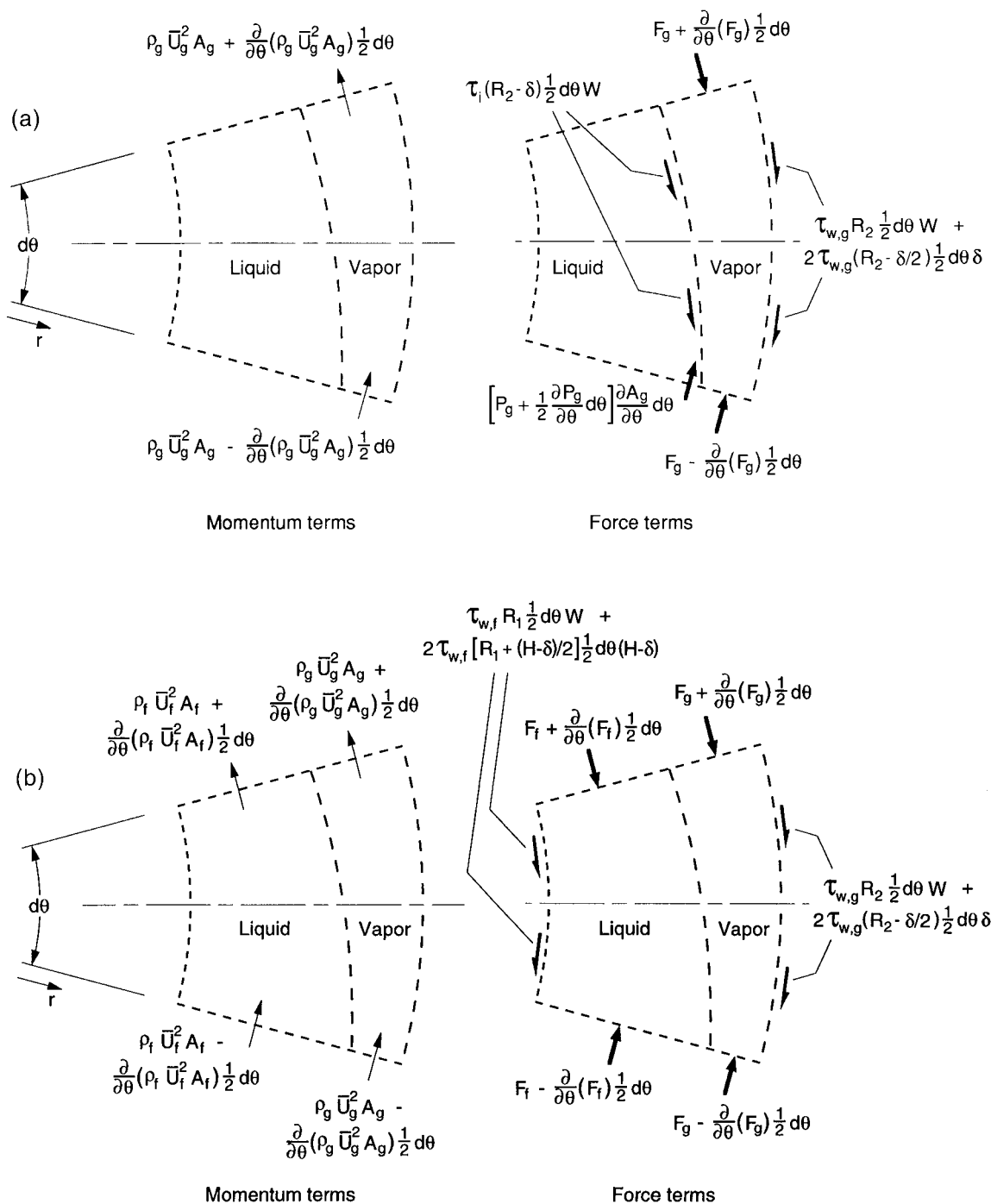
where

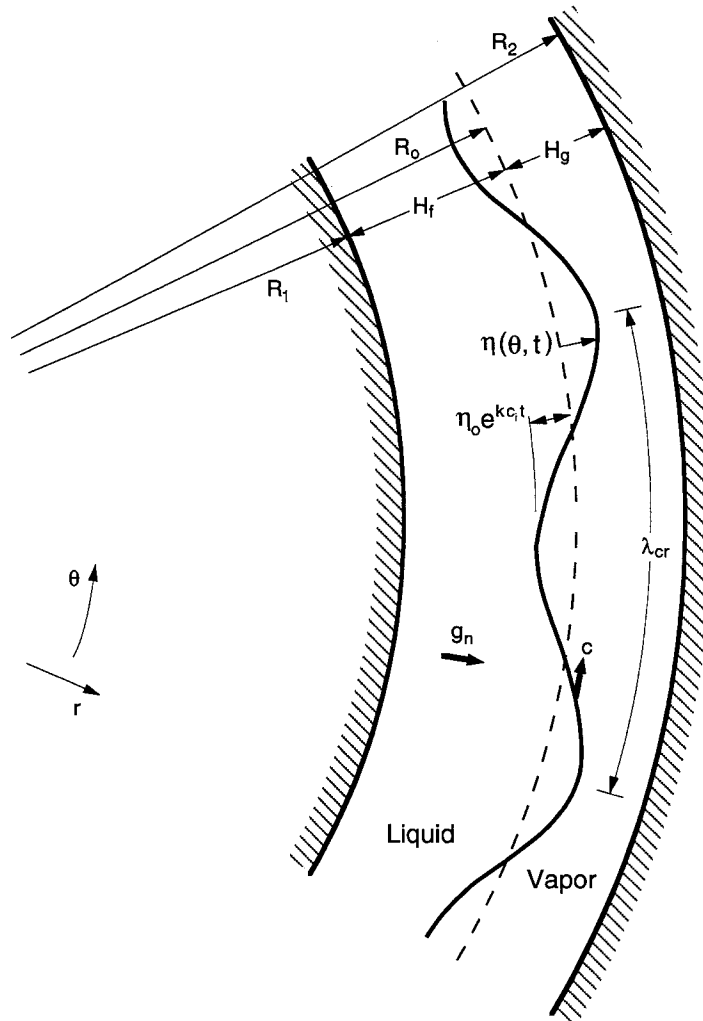Fig. 7. Momentum and force terms for (a) vapor and (b) channel control volumes in curved, rectangular channel.

Fig. 8. Wavy interfacial boundary between the liquid and vapor phases in a curved, rectangular channel.

$$\left(-\frac{\mathrm{d}P_i}{\mathrm{d}z}\right)_{\mathrm{A}} = \frac{1}{H}\frac{\mathrm{d}}{\mathrm{d}z}[\rho_g \bar{U}_g^2 \delta + \rho_f \bar{U}_f^2 (H-\delta)] \tag{17}$$

$$\left(-\frac{\mathrm{d}P_i}{\mathrm{d}z}\right)_{\mathrm{F}} = \tau_{\mathrm{w},g}\left(\frac{1}{H} + 2\frac{\delta}{WH}\right)$$
$$+ \tau_{\mathrm{w},f}\left(\frac{1}{H} + 2\frac{H-\delta}{WH}\right)\frac{R_1}{R_2} \tag{18}$$

$$\left(-\frac{\mathrm{d}P_i}{\mathrm{d}z}\right)_{\mathrm{C}} = \frac{\rho_f \bar{U}_f^2}{H}\frac{H-\delta}{R_2-\delta}\frac{\mathrm{d}\delta}{\mathrm{d}z}$$
$$+ 2\frac{\rho_f \bar{U}_f}{H}\left[R_1 \ln\left(\frac{R_2-\delta}{R_1}\right) - (H-\delta)\right]\frac{\mathrm{d}\bar{U}_f}{\mathrm{d}z}. \tag{19}$$

These are analogous to the pressure gradient expressions derived for the straight channel [9]. Comparison reveals that an additional mechanism is responsible for pressure losses in the curved channel. $(-\mathrm{d}P_i/\mathrm{d}z)_{\mathrm{C}}$ is referred to as the centrifugal or curvature component and arises due to the presence of the radial pressure gradient. As R_1 and R_2 become large ($R_1 \to \infty$ and $R_2 \to \infty$) the centrifugal component goes to zero and the remaining components of pressure gradient become identical to those derived for the straight channel.

The wall and interfacial shear terms are evaluated in a manner similar to the straight channel analysis,

$$\tau_{\mathrm{w},k} = \frac{1}{2}\rho_k \bar{U}_k^2\left(\frac{f_k}{4}\right) \tag{20}$$

$$\tau_i = \frac{1}{2}\rho_g(\bar{U}_g - \bar{U}_f)^2 C_{f,i} \tag{21}$$

where k indicates the phase and i the interface. Friction factors must be appropriately chosen for curved flow. They may be evaluated using the correlation developed by Mishra and Gupta [13],

$$f_k = 0.079\left[\frac{\rho_k \bar{U}_k D_{h,k}}{\mu_k}\right]^{-0.25} + 0.0075\left[\frac{D_{h,k}}{2R_2}\right]^{0.5} \tag{22}$$

or the relationship by Ito [14],

$$f_k = f_{str}\left[\frac{\rho_k \bar{U}_k D_{h,k}}{\mu_k}\right]^{1/20}\left[\frac{D_h}{2R_2}\right]^{1/10}. \tag{23}$$

f_{str} is the friction factor for the corresponding phase in the straight channel and $D_{h,k}$ is the phase hydraulic diameter. The interfacial friction coefficient is best represented by a constant value of $C_{f,i} = 0.5$, as supported by the work of Galloway and Mudawar [8].

The procedure for determining $\bar{U}_g$, $\bar{U}_f$ and δ is analogous to that presented for the straight channel [9] where vapor thickness is iterated upon until the two pressure gradients are equal (phases are in mechanical equilibrium at the interface). Values for $\bar{U}_g$, $\bar{U}_f$ and δ at each z location are then used in the instability analysis.

5.2. Instability analysis

Instability analysis for curved flow is complicated by the fact that pressure increases radially outward and classical stability theory for straight channels [15,16] does not address this issue. Galloway and Mudawar [2] presented an approach accounting for the radial pressure gradient which is outlined here with reference to the liquid–vapor interface depicted for curved flow in Fig. 8.

Under the assumption of incompressible, irrotational flow, the velocity field within each phase may be determined by employing potential flow theory and solving the Laplace equation for liquid and vapor velocity potentials. The problem is linearized by expressing each velocity component as the sum of a mean value and a small perturbation from the mean. Since there is no mean motion in the radial direction, the radial velocity component is just the perturbation term. The mean potentials are easily constructed to recover the mean components, as determined from the separated flow analysis, upon differentiation. Solution of the perturbation potentials require application of two sets of boundary conditions: (1) radial components of velocity at the inner and outer walls are zero, and (2) radial velocity components of each phase are equal at the interface.

The procedure for analyzing flow stability is to first solve for the perturbation potentials by applying the boundary conditions. Then the total velocity potentials will be known. These potentials then yield the velocity field which is used in the Bernoulli equation to determine the pressure field. This allows for the calculation of the pressure difference across the interface which is responsible for curvature and, consequently, interfacial instability. The pressure difference leads to an equation for interfacial wave speed which then provides the criterion for instability.

Solving for the velocity field then utilizing the Bernoulli equation leads to an expression for interfacial pressure difference given by

$$\begin{aligned}P_f - P_g = \Big[&\rho_f'''(\bar{U}_{f,i} - c)^2 + \rho_g'''(\bar{U}_{g,i} - c)^2 \\ &- (\rho_f - \rho_g)\frac{g_n}{k}\Big]k\eta_0\, e^{ik(\theta R_0 - ct)}\end{aligned} \tag{24}$$

with the modified density terms, ρ_f''' and ρ_g''', defined [2] by

$$\rho_f''' = \rho_f\left[\frac{\left(\frac{R_0}{R_1}\right)^{2kR_0} + 1}{\left(\frac{R_0}{R_1}\right)^{2kR_0} - 1}\right] \tag{25a}$$

and

$$\rho_g''' = \rho_g\left[\frac{\left(\frac{R_0}{R_2}\right)^{2kR_0} + 1}{1 - \left(\frac{R_0}{R_2}\right)^{2kR_0}}\right]. \tag{25b}$$

The interface has been assumed periodic which, allowing for a complex wave speed $c = c_r + ic_i$, is expressed by

$$\eta(\theta,t) = \eta_0\, e^{ik(\theta R_0 - ct)} = \eta_0\, e^{c_i kt}\, e^{ik(\theta R_0 - c_r t)} \tag{26}$$

where only the real part of $\eta(\theta, t)$ describes the actual interface; the imaginary part will provide information regarding wave stability.

Pressure across a wavy interface with mild curvature $(\partial\eta/\partial z \ll 1)$ may also be approximated by the product of surface tension and curvature,

$$P_f - P_g = -\sigma\frac{\partial^2\eta}{\partial(R_0\theta)^2} = -\frac{\sigma}{R_0^2}\frac{\partial^2\eta}{\partial\theta^2} \tag{27}$$

The negative sign here arises from the different orientation of the coordinate system with respect to the phases in comparison to the straight channel. Substituting the interface equation given by Eq. (26)
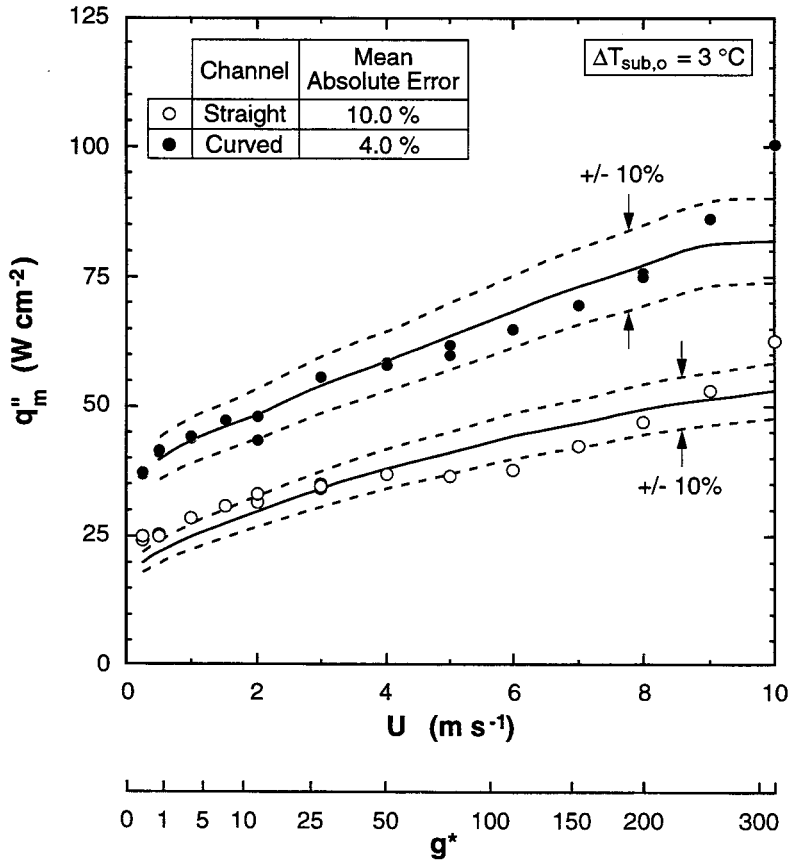
Fig. 9. CHF data and model predictions for near-saturated conditions in straight and curved channels.

into (27) and equating the two expressions for pressure difference [Eqs. (24) and (27)] yield a quadratic expression for the wave speed, c.

$$[\rho_f''' + \rho_g''']c^2 - 2[\rho_f'''\bar{U}_{f,i} + \rho_g'''\bar{U}_{g,i}]c + \left[\rho_f'''\bar{U}_{f,i}^2 + \rho_g'''\bar{U}_{g,i}^2 - (\rho_f - \rho_g)\frac{g_n}{k} - \sigma k\right] = 0. \tag{28}$$

Solving for the wave speed yields

$$c = \frac{\rho_f'''\bar{U}_{f,i} + \rho_g'''\bar{U}_{g,i}}{\rho_f''' + \rho_g'''} \pm \sqrt{\frac{\sigma k}{\rho_f''' + \rho_g'''} - \frac{\rho_f'''\rho_g'''(\bar{U}_{g,i} - \bar{U}_{f,i})^2}{(\rho_f''' + \rho_g''')^2} + \frac{(\rho_f - \rho_g)}{(\rho_f''' + \rho_g''')}\frac{g_n}{k}} \tag{29}$$

The expression for the interface, Eq. (26), indicates the conditions for stability. For $c_i < 0$, the amplitude diminishes leading to a stable interface, while for $c_i > 0$ it is unstable. The critical wavelength is defined for the condition of neutral stability, when $c_i = 0$. An imaginary component of wave speed arises when the radicand in Eq. (29) is negative. Therefore, setting this term equal to zero results in the desired expression for critical wavelength, λ_{cr}.

$$k_{cr} = \frac{2\pi}{\lambda_{cr}} = \frac{\rho_f'''\rho_g'''(\bar{U}_{g,i} - \bar{U}_{f,i})^2}{2\sigma(\rho_f''' + \rho_g''')} + \sqrt{\left[\frac{\rho_f'''\rho_g'''(\bar{U}_{g,i} - \bar{U}_{f,i})^2}{2\sigma(\rho_f''' + \rho_g''')}\right]^2 - \frac{(\rho_f - \rho_g)g_n}{\sigma}} \tag{30}$$

This expression for critical wavelength in the curved channel is identical to that for the straight channel allowing for the sign change on g_n (due to coordinate system definition), the different definitions for modified density terms and the use of interfacial phase velocities ($\bar{U}_{g,i}$, $\bar{U}_{f,i}$).

If the body forces are negligible, $g_n = 0$ and the critical wavelength is given by

$$\lambda_{cr} = \frac{2\pi\sigma(\rho_f''' + \rho_g''')}{\rho_f'''\rho_g'''(\bar{U}_{g,i} - \bar{U}_{f,i})^2} \qquad (31)$$

5.3. Solution procedure

As discussed previously, the CHF model development is similar to that presented for long, straight heaters with curvature effects appearing in the separated flow model, instability analysis and flow visualization results. Predictions of CHF require an iterative process incorporating the four model components. First, upon selecting appropriate velocity, subcooling and property values, an initial estimate for CHF is made. The separated flow model is then utilized to calculate phase velocities [Eqs. (10) and (11)] and vapor thickness (iterating parameter) which are required by the instability analysis to determine the critical wavelength, λ_{cr} [Eq. (31)], and length of continuous upstream wetting front, z^* [Eq. (1)]. Since the wetting length remains proportional to the vapor wavelength, the product $(l_j n_j)$ simplifies the energy balance by eliminating explicit dependence on either l_j or λ_j. Next, the average interfacial pressure difference at z^* [Eq. (6)] is calculated and used in evaluating the lift-off flux at z^* [Eq. (7)]. This flux is a function of the pressure difference, subcooling, vapor thickness and critical wavelength. The liquid-to-vapor length ratio, b, represents a key contribution of flow visualization.

The energy balance then yields a value for the critical heat flux [Eq. (8)]. If this value is sufficiently close to the estimate which initiated the process, CHF is predicted. If not, the estimate is updated using the bisection method and the process repeated until the iteration converges on a CHF value.

5.4. Model predictions

The CHF model was applied to the straight and curved channels for near-saturated conditions over the entire range of velocity for which data were obtained. Properties were assumed constant since experimental temperature and pressures varied only slightly. Phase velocities and vapor layer thickness as determined by the separated flow model showed little sensitivity to the small subcooling variations along the flow direction. This being the case, subcooling was fixed at the inlet value for the near-saturated case to simplify model calculations and implementation. Theoretically, this means that the liquid bulk temperature remained constant; though not exact, it represents an acceptable approximation for this case.

Flow visualization aided in the construction of the

model in that it quantified the liquid-to-vapor length ratio which was observed to be approximately 0.20 and 0.27 for straight and curved flow, respectively, at near-saturated conditions. These ratios remained constant for all segments along the respective heaters indicating that as the wavelength grew so did the wetting length in a proportionate amount.

Fig. 9 shows the model predictions for CHF in a concave-heated channel at near-saturated conditions for the range of velocity and corresponding centripetal acceleration tested. The model estimates the experimental data to within a mean absolute error of only 4.0% for velocities greater than 0.25 m s^{-1}. The largest error is 18.6% corresponding to $U = 10$ m s^{-1}. Also shown are the straight channel results in which case the model predictions utilized the appropriate separated flow model, instability analysis and flow visualization results, as previously presented by the present authors [9]. The mean absolute error in this case is 10.0%. The curved flow predictions indicate an increasing CHF with increasing velocity as well as an increase in CHF relative to that predicted for straight flow, as would be intuitively expected. Therefore, the model offers predictions for CHF that are both intuitively consistent and numerically accurate, lending support for the assumptions of the derivation. It should be noted, however, that at the high end of the velocity range the data seem to increase at a greater rate than predicted, with the CHF value at $U = 10$ m s^{-1} underpredicted. This may indicate that the model is near its limit of applicability in terms of velocity and should be applied with caution for velocities greater than 10 m s^{-1}. This discrepancy may reflect loss of fidelity in assumptions regarding constant properties and bulk temperature, constant liquid-to-vapor length ratio, mild interfacial curvature, frictional coefficients and energy balance based on discretized heated length.

When applied to subcooled conditions ($\Delta T_{sub,o} = 29°C$), the curved model predicted critical heat fluxes with less accuracy, which was also true for the straight CHF model [9]. Though predicted CHF increased with increasing velocity and increased relative to straight flow, the predictions did not capture the slope of the data resulting in a mean absolute error of 18.6%. This is due to condensation at the liquid–vapor interface which the separated flow model regards as negligible, which is reasonable only for near-saturated conditions. Interfacial condensation should therefore be carefully addressed in future subcooled flow boiling CHF models.

6. Conclusions

A CHF model for flow in a curved, rectangular channel was developed drawing on the interfacial lift-

off model of Galloway and Mudawar [8] and the model for long, straight channels presented by the present authors [9]. Key conclusions are as follows:

1. Flow visualization revealed that at conditions prior to CHF, vapor assumes a wavy, periodic distribution along the heated, concave wall near the heater inlet. The buoyancy forces present in curved flow pulled the vapor inward leading to greater measured vapor heights in the inlet region as compared to corresponding locations in the straight channel. This resulted in greater interfacial curvature which produced a greater interfacial pressure force to resist the vapor momentum, thereby delaying interfacial lift-off and increasing CHF for curved flow.
2. The ability of liquid to rewet the surface in the presence of vapor is indicated by the ratio of liquid wetting length to vapor wavelength. This ratio increased to 0.27 for curved flow, from the straight flow value of 0.20, based on the flow visualization measurements at near-saturated conditions.
3. The curved channel model developed in this study as an extension of the interfacial lift-off model first proposed by Galloway and Mudawar [8] accurately predicts CHF data (mean absolute error of 4.0%) obtained over a broad range of velocity ($U = 0.5$–10 m s^{-1}) on a long heater at near-saturated ($\Delta T_{sub,o} = 3°C$) conditions. The present work validates the Galloway and Mudawar model's applicability (with slight modifications) for long heater ($L \approx 100$ mm) and high accelerations (up to 315g_e). The model represents a mechanistically-based tool which incorporates a separated flow model, interfacial instability analysis, energy balance, lift-off criterion and flow visualization description.
4. The model for long, curved channels is consistent with the model developed by the present authors for long, straight rectangular channels. Development is the same with curvature influencing the predictions through the separated flow model, instability analysis and flow visualization results.
5. The inability of the separated flow model to account for interfacial condensation limits the model's applicability to only near-saturated conditions. Condensation needs to be carefully addressed in any future models of highly subcooled flow boiling CHF.

Acknowledgements

The authors are grateful for the support of the Office of Basic Energy Sciences of the U.S. Department of Energy (Grant No. DE-FG02-93ER14394.A003). Financial support for the first author was provided through the Air Force Palace Knight Program.

References

[1] T.G. Hughes, D.R. Olson, Critical heat fluxes for curved surfaces during subcooled flow boiling. U.S. National Heat Transfer Conference, vol. 3, San Francisco, CA, 1975, pp. 122–130.
[2] J.E. Galloway, I. Mudawar, A theoretical model for flow boiling CHF from short concave heaters, ASME Journal of Heat Transfer 117 (1995) 698–707.
[3] C.B. Gu, L.C. Chow, J.E. Beam, Flow boiling in a curved channel, in: R.J. Goldstein, L.C. Chow, E.E. Anderson (Eds.), Heat Transfer in High Energy/High Heat Flux Applications, vol. 119, ASME HTD, 1989, pp. 25–32.
[4] J.C. Sturgis, I. Mudawar Assessment of CHF enhancement mechanisms in a curved, rectangular channel subjected to concave heating. ASME Journal of Heat Transfer, in press.
[5] J.E. Leland, L.C. Chow, Effect of channel height and radius of curvature on forced convective boiling in a rectangular channel. 30th Aerospace Science Meeting and Exhibit, Reno, NV, 1992.
[6] P.S. Wu, T.W. Simon, Critical heat flux and subcooled flow boiling with small heated regions on straight and concave-curved walls. 10th International Heat Transfer Conference, vol. 7, Brighton, UK, 1994, pp. 569–574.
[7] W.R. Gambill, N.D. Greene, Boiling burnout with water in vortex flow, Chemical Engineering Progress 54 (1958) 68–76.
[8] J.E. Galloway, I. Mudawar, CHF mechanisms in flow boiling from a short heated wall—Part II. Theoretical CHF model., International Journal of Heat and Mass Transfer 36 (1993) 2527–2540.
[9] J.C. Sturgis, I. Mudawar, Critical heat flux in a long, rectangular channel subjected to one-sided heating—II. Analysis of CHF data. International Journal of Heat and Mass Transfer 42 (1999) 1849–1862.
[10] J.E. Galloway, I. Mudawar, CHF mechanism in flow boiling from a short heated wall—Part I. Examination of near-wall conditions with the aid of photomicrography and high-speed video imaging, International Journal of Heat and Mass Transfer 36 (1993) 2511–2526.
[11] C.O. Gersey, I. Mudawar, Effects of heater length and orientation on the trigger mechanisms for near-saturated flow boiling critical heat flux—I. Photographic study and statistical characterization of the near-wall interfacial features, International Journal of Heat and Mass Transfer 38 (1995) 629–641.
[12] J.C. Sturgis, I. Mudawar, Critical heat flux in a long, rectangular channel subjected to one-sided heating—I. Flow visualization. International Journal of Heat and Mass Transfer 42 (1999) 1835–1847.

[13] P. Mishra, S.N. Gupta, Momentum transfer in curved pipes, 1. Newtonian fluids, Industrial Engineering Chemical Process Design and Development 18 (1979) 130–137.

[14] H. Ito, Friction factors for turbulent flow in curved pipes, Journal of Basic Engineering 13 (1959) 123–134.

[15] H. Lamb, Hydrodynamics, Dover, New York, 1945.

[16] L.M. Milne-Thomson, Theoretical Hydrodynamics, MacMillan, New York, 1960.